

# Towards the ultimate PMT waveform analysis

Dacheng Xu<sup>a,b,c</sup>, Benda Xu<sup>\*a,b,c,d</sup>, Erjin Bao<sup>e,f</sup>, Yiyang Wu<sup>a,b,c</sup>, Aiqiang Zhang<sup>a,b,c</sup>, Yuyi Wang<sup>a,b,c</sup>, Geliang Zhang<sup>g</sup>, Yu Xu<sup>h</sup>, Ziyi Guo<sup>a,b,c</sup>, Jihui Pei<sup>†i,2</sup>, Hanyang Mao<sup>j</sup>, Jiashuo Liu<sup>j</sup>, Zhe Wang<sup>a,b,c</sup>, and Shaomin Chen<sup>a,b,c</sup>

<sup>a</sup>*Department of Engineering Physics, Tsinghua University, Beijing, China*

<sup>b</sup>*Center for High Energy Physics, Tsinghua University, Beijing, China*

<sup>c</sup>*Key Laboratory of Particle & Radiation Imaging (Tsinghua University), Ministry of Education, China*

<sup>d</sup>*Kavli Institute for the Physics and Mathematics of the Universe, UTIAS, the University of Tokyo, Japan*

<sup>e</sup>*National Institute of Informatics, Tokyo, Japan*

<sup>f</sup>*Department of Informatics, The Graduate University for Advanced Studies (SOKENDAI), Tokyo, Japan*

<sup>g</sup>*School of Securities and Futures, Southwestern University of Finance and Economics, Chengdu, China*

<sup>h</sup>*School of Physics, Sun Yat-Sen University, Guangdong, China*

<sup>i</sup>*Department of Physics, Tsinghua University, Beijing, China*

<sup>j</sup>*Department of Computer Science and Technology, Tsinghua University, Beijing, China*

## Abstract

Photomultiplier tube (PMT) voltage waveforms are the raw data of many neutrino and dark matter experiments. Waveform analysis is the cornerstone of data processing. We evaluate the performance of all the waveform analysis algorithms known to us and find fast stochastic matching pursuit the best in accuracy. Significant time (up to  $\times 2$ ) and energy (up to  $\times 1.04$ ) resolution boosts are attainable with fast stochastic matching pursuit, approaching theoretical limits. Other methods also outperform the traditional threshold crossing approach in time resolution.

KEYWORDS: PMT, Neutrino detector, Data analysis

## Contents

<b>1</b>	<b>Introduction</b>	<b>2</b>
<b>2</b>	<b>Scope and Motivation</b>	<b>2</b>
2.1	Light curve	2
2.2	Single PE response	3
2.3	Measurement of incident light	4
2.3.1	Time $t_0$	5
2.3.2	Intensity $\mu$	6
2.3.3	Shape $\phi(\cdot)$	6
<b>3</b>	<b>Algorithms and their performance</b>	<b>6</b>
3.1	Evaluation criteria	6
3.1.1	Kullback-Leibler divergence	7
3.1.2	Residual sum of squares	7
3.1.3	Wasserstein distance	8
3.2	Heuristic methods	8
3.2.1	Waveform shifting	8

<sup>\*</sup>Corresponding author. orv@tsinghua.edu.cn

<sup>†</sup>Current address: School of Physics, Peking University, Beijing, China.

3.2.2	Peak finding	9
3.3	Deconvolution	9
3.3.1	Fourier deconvolution	9
3.3.2	Richardson-Lucy direct demodulation	10
3.4	Convolutional neural network	11
3.5	Regression analysis	12
3.5.1	Direct charge fitting	12
3.5.2	Markov chain Monte Carlo	13
3.5.3	Fast stochastic matching pursuit	14
<b>4</b>	<b>Summary and discussion</b>	<b>16</b>
4.1	Performance	16
4.2	Charge fidelity and sparsity	18
4.3	Inference of incident light	19
<b>5</b>	<b>Conclusion</b>	<b>21</b>

## 1 Introduction

Waveform analysis of photomultiplier tubes (PMT) is ubiquitous in fluid-based neutrino and dark matter experiments. Via hit time and number of photoelectrons (PE), it provides a more accurate measurement of time and intensity of incident light on a PMT, improves event reconstruction, particle identification and definition of fiducial volume, thus promoting the physics prospect.

In Super-Kamiokande [1], SNO [2] and Daya Bay [3], the time (TDC) and charge (QDC) to digital converters recorded the threshold crossing times and integrated charges of PMT waveforms. Experimentalists deployed fast analog-to-digital converters to record full PMT waveforms in KamLAND [4], Borexino [5], XMASS [6], XENON1T [7]. This technology advancement opened the flexibility of offline waveform analysis after data acquisition. Nevertheless, limited by data volume and computational efficiency, early adopters emulated TDC/QDC in software with threshold and integration algorithms. Only recently have people explored methods to extract charge and hit time of each PE [8]. However, there is still a great potential for improvements. We shall see that TDC suffers from the ignorance of the second and subsequent PEs (section 2.3.1), and QDC is hindered by charge fluctuation (section 2.3.2).

Our mission on waveform analysis is to infer PEs from a waveform, consequently the incident light intensity over time. The latter is the input to event reconstruction. We shall go through all the known methods and strive towards the ultimate algorithm that retains all the available information in the data. In section 2, we discuss the principles of PE measurement in PMT-based detectors to justify the toy MC setup. We then introduce waveform analysis algorithms and characterize their performance. In section 3, Finally, in section 4, we discuss the impact on event reconstruction by comparing the time and intensity resolutions.

## 2 Scope and Motivation

In this section, we discuss the vital importance of waveform analysis for incident light measurements in PMT-based experiments.

### 2.1 Light curve

A particle interacts with matter and deposits energy when passing through the detector. Part of such energy converts into visible Cherenkov or scintillation photons. The *light curve* is the time evolution of light intensity at a PMT,

$$\mu\phi(t - t_0) \tag{1}$$

where  $\mu$  is the intensity factor,  $t_0$  is the time shift factor, and  $\phi(\cdot)$  is the normalized shape function. For simplicity, we parameterize the scintillation light curve as an exponential distribution and the Cherenkov one by a Dirac delta function. It is convenient to model the PMT transit time spread (TTS) in  $\phi(t)$  as a Gaussian smear, giving an *ex-Gaussian* or *exponentially modified Gaussian* [9],

$$\phi(t) = \frac{1}{2\tau_\ell} \exp\left(\frac{\sigma_\ell^2}{2\tau_\ell^2} - \frac{t}{\tau_\ell}\right) \left[1 - \text{erf}\left(\frac{\sigma_\ell}{\sqrt{2}\tau_\ell} - \frac{t}{\sqrt{2}\sigma_\ell}\right)\right], \quad (2)$$

where subscript  $\ell$  stands for “light curve” and  $\sigma_\ell$  encodes the timing uncertainty mainly from TTS.  $\phi(t)$  of Cherenkov light is a pure Gaussian by taking  $\tau_\ell \rightarrow 0$ . Figure 1 illustrates 3 examples of  $\phi(t)$ .

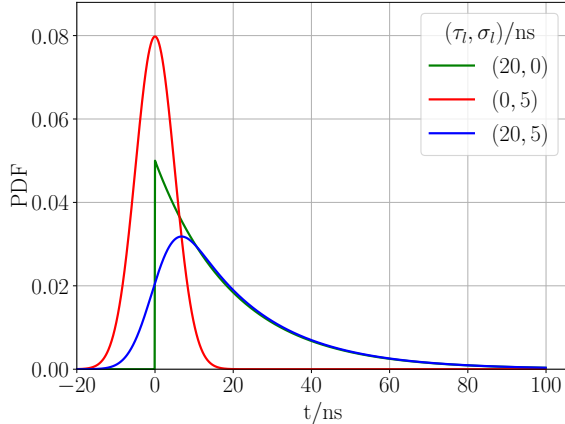
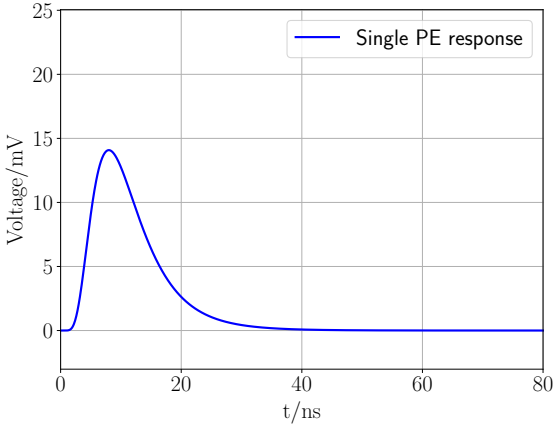


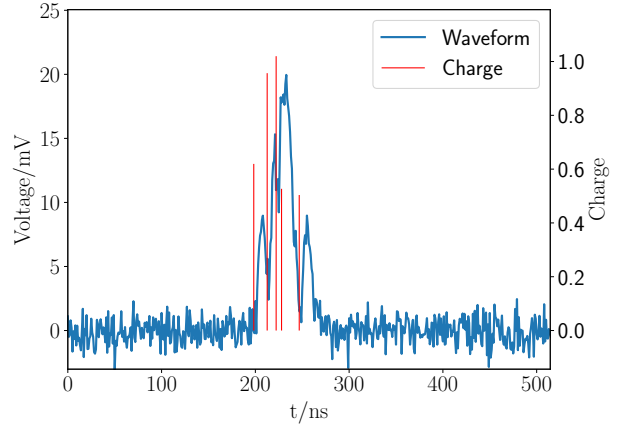
Figure 1: Effective light curves in the three settings. A scintillator paired with ultra-fast photo-sensors gives the green curve with  $\tau_\ell \gg \sigma_\ell$ . A fast Cherenkov detector by the red curve has  $\tau_\ell \ll \sigma_\ell$ . The blue curve combining  $\tau_\ell = 20$  ns and  $\sigma_\ell = 5$  ns represents a typical scintillation detector. We can regard  $\phi(t)dt$  as a probability density function (PDF at the vertical axis) of PE times.

## 2.2 Single PE response

A PE induced by a photon at the PMT photocathode is then accelerated, collected, and amplified into  $\sim 10^7$  electrons, forming a voltage pulse  $V_{\text{PE}}(t)$  in the PMT output.



(a) Single PE response  $V_{\text{PE}}(t)$  in eq. (3).



(b) PE pile-up and white noise in an PMT waveform.

Figure 2: A single PE from a PMT induces a voltage pulse in (a). Multiple PEs pile up at a PMT form an input waveform  $w(t)$  in (b), when PEs are barely visually separable from each other. Output charge  $\hat{\mathbf{t}}, \hat{\mathbf{q}}$  also in (b), which we will discuss in section 3.

S. Jetter et al. [10] parameterize  $V_{\text{PE}}(t)$  as,

$$V_{\text{PE}}(t) = V_0 \exp \left[ -\frac{1}{2} \left( \frac{\log(t/\tau_{\text{PE}})}{\sigma_{\text{PE}}} \right)^2 \right], \quad (3)$$

where shape parameters  $\tau_{\text{PE}} = 8 \text{ ns}$ ,  $\sigma_{\text{PE}} = 0.5 \text{ ns}$  and  $V_0 = 14.08 \text{ mV}$ , see figure 2a. A sample of PEs from the light curve  $\phi(t)$  in eq. (2) can be formulated as several delta functions, also known as sparse spike train [11],

$$\tilde{\phi}(t) = \sum_{i=1}^{N_{\text{PE}}} q_i \delta(t - t_i), \quad (4)$$

where  $N_{\text{PE}}$  is the number of PEs following Poisson distribution with parameter  $\mu$ .  $t_i$  is the hit time of the  $i$ -th PE,  $q_i$  is the relative charge of the  $i$ -th PE from charge distribution  $\mathcal{N}(1, \sigma_q^2)$ .  $\sigma_q$  is set to 0.25 in our simulation.

A noise-free waveform  $\tilde{w}(t)$  is a convolution of  $\tilde{\phi}(t)$  and  $V_{\text{PE}}(t)$ , and the PMT voltage output waveform  $w(t)$  is a time series modeled by the sum of  $\tilde{w}(t)$  and a Gaussian white noise  $\epsilon(t)$ ,

$$\begin{aligned} \tilde{w}(t) &= \tilde{\phi}(t) \otimes V_{\text{PE}}(t) \\ w(t) &= \tilde{w}(t) + \epsilon(t) = \sum_{i=1}^{N_{\text{PE}}} q_i V_{\text{PE}}(t - t_i) + \epsilon(t). \end{aligned} \quad (5)$$

See figure 2b for an example.

We do not dive into pedestals or saturation for simplicity. We also assumed the single PE response  $V_{\text{PE}}(t)$ , the variance of charge  $\sigma_q^2$  and the distribution of noise  $\epsilon(t)$  are known. Otherwise, they should be measured by PMT calibrations and modeled with uncertainty.

### 2.3 Measurement of incident light

We see in figure 2b that pile-ups and noises hinder the time  $t_i$  and charge  $q_i$  of the PEs. Fortunately, event reconstruction only takes the time shift  $t_0$  and the intensity  $\mu$  in eq. (1) as inputs, where  $t_0$  carries the time of flight information and  $\mu$  is the expected  $N_{\text{PE}}$  in a real detector. All the uncertainties of  $\hat{t}_i$ ,  $\hat{q}_i$  and  $\hat{N}_{\text{PE}}$  are reflected in  $\hat{t}_0$  and  $\hat{\mu}$ . In this article, we denote  $\hat{x}$  as an estimator for the corresponding variable  $x$  if not otherwise specified. Classical TDC extracts the waveform's

threshold crossing time  $\hat{t}_{1st}$  to approximate the hit time of the first PE, while QDC extracts total charge  $Q$  from waveform integration to estimate  $\mu$  by  $\hat{\mu}_Q$ .

### 2.3.1 Time $t_0$

$\hat{t}_{1st}$  is a biased estimator of  $t_0$ . It is affected by the light intensity  $\mu$ , which we shall show in figure 15a and section 4.3. We define the resolution  $\sigma_{1st}$  for a batch of waveforms as the standard deviation of  $\Delta t_0 = \hat{t}_{1st} - t_0$ . From a hypothetical perfect measurement of  $t_i$ , we define an ideal maximum likelihood estimator (MLE)  $\hat{t}_{ALL}$  to capture time information of all the PEs,

$$\hat{t}_{ALL} = \arg \max_{t_0} \prod_{i=1}^{N_{PE}} \phi(t_i - t_0). \quad (6)$$

The corresponding  $\sigma_{ALL}$  is the lower bound of time resolution.

To characterize  $\hat{t}_{1st}$  and  $\hat{t}_{ALL}$ , we scan  $\mu$  from 0 to 30 for each light curve in figure 1. We generate a sample of  $10^4$  waveforms having at least 1 PE for every triplet of  $(\tau_\ell, \sigma_\ell, \mu)$ . Figure 3 shows that  $\sigma_{1st}$  equals  $\sigma_{ALL}$  when  $\tau_\ell \gg \sigma_\ell$ , because  $\hat{t}_{ALL}$  reduces to  $\hat{t}_{1st} (= \min_i t_i)$  for an exponential light curve. For  $\mu \rightarrow 0$ ,  $\sigma_{1st}$  and  $\sigma_{ALL}$  are also equal because at most 1 PE is available. TDC is effective in those cases.

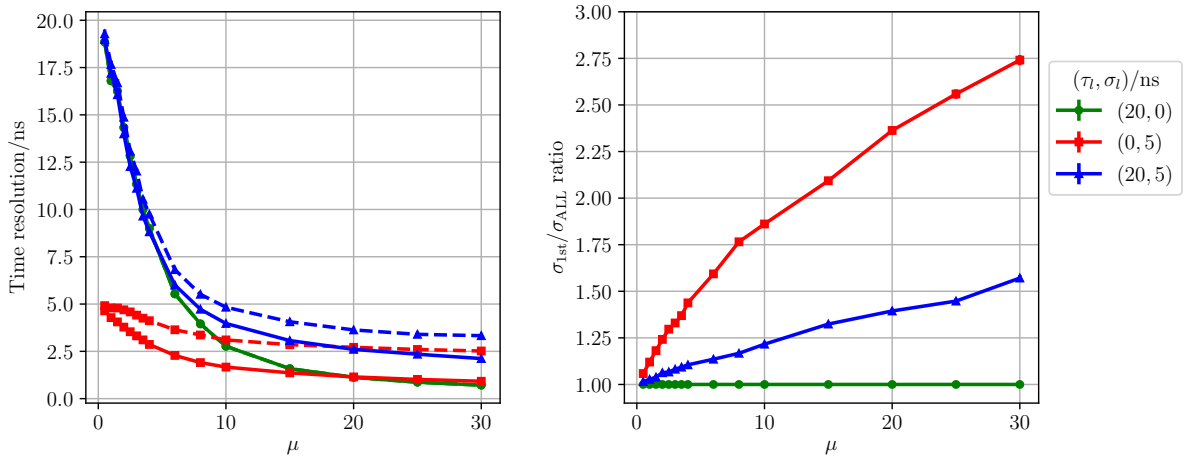


Figure 3: Time resolution comparisons between  $\hat{t}_{ALL}$  (solid lines, when using the information of all PEs) and  $\hat{t}_{1st}$  (dashed lines, using the first PE instead of the threshold crossing time to eliminate the influence from TDC). The difference is manifested especially when  $\sigma_\ell$  and  $\mu$  are large. The three cases of  $(\tau_\ell, \sigma_\ell)/\text{ns}$  represent the scintillation with ultra-fast PMTs (20, 0), Cherenkov (0, 5) and scintillation coupled with PMT TTS (20, 5). The performance of waveform analysis lies between  $\sigma_{1st}$  and  $\sigma_{ALL}$ .

Nevertheless, for  $\sigma_\ell > 0$  and  $\mu > 0$ , the  $\sigma_{1st}$  significantly deteriorates from  $\sigma_{ALL}$ . For Cherenkov and scintillation experiments with non-negligible PMT TTS and occupancy, we shall explore more sophisticated waveform analysis algorithms to go beyond  $\hat{t}_{1st}$  and recover the accuracy of  $\hat{t}_{ALL}$  in eq. (6) from waveform in eq. (5).

### 2.3.2 Intensity $\mu$

Noting  $Q_0 = \int V_{\text{PE}}(t)dt$ , the charge estimator  $\hat{\mu}_Q$  for QDC is

$$\begin{aligned}\hat{\mu}_Q &= \frac{1}{Q_0} \int w(t)dt = \frac{1}{Q_0} \sum_{i=1}^{N_{\text{PE}}} \int [q_i V_{\text{PE}}(t - t_i) + \epsilon(t)] dt \\ &= \sum_{i=1}^{N_{\text{PE}}} q_i + \frac{1}{Q_0} \int \epsilon(t)dt.\end{aligned}\tag{7}$$

Its expectation and variance are,

$$\begin{aligned}\mathbb{E}[\hat{\mu}_Q] &= \mathbb{E}[N_{\text{PE}}] \\ \text{Var}[\hat{\mu}_Q] &= \text{Var} \left[ \sum_{i=1}^{N_{\text{PE}}} q_i \right] + \text{Var} \left[ \frac{1}{Q_0} \int \epsilon(t)dt \right] \\ &= \mathbb{E}[q^2] \text{Var}(N_{\text{PE}}) + \frac{T}{Q_0^2} \sigma_{\epsilon}^2 \\ &= (1 + \sigma_q^2) \text{Var}(N_{\text{PE}}) + \frac{T}{Q_0^2} \sigma_{\epsilon}^2.\end{aligned}\tag{8}$$

where the first term of the variance is the that of a compound Poisson distribution, and  $T$  in the second one is a constant proportional to the time window. Resolution of  $\hat{\mu}_Q$  is affected by the Poisson fluctuation of  $N_{\text{PE}}$ , the charge resolution of a PE  $\sigma_q$  and the white noise  $\sigma_{\epsilon}$ .

Sometimes we mitigate the impact of  $\sigma_q$  and  $\sigma_{\epsilon}$  by rounding  $\hat{\mu}_Q$  to integers. It works well for  $N_{\text{PE}} \leq 1$ , which is equivalently a hit-based 0-1  $\mu$  estimator  $\hat{\mu}_{\text{hit}}$ . But for  $N_{\text{PE}} \geq 2$ , it is hard to interpret  $\hat{\mu}_Q$  rounding by physics principles and  $\hat{\mu}_{\text{hit}}$  does not gain any additional information from the extra PEs.

The goal of waveform analysis is to eliminate the impact of  $\sigma_q$  and  $\sigma_{\epsilon}$  as much as possible. The pure Poisson fluctuation of  $N_{\text{PE}}$  is the resolution lower bound  $\sigma_{\mu} = \sqrt{\mu}$  of any  $\mu$  estimator.

### 2.3.3 Shape $\phi(\cdot)$

The shape of a light curve is determined by light emission time profile, PMT timing and light propagation, including refraction, reflection, dispersion and scattering.  $\phi(\cdot)$  thus depends on event locations. In this article, we model  $\phi(\cdot)$  by eq. (2) for simplicity and leave the  $\phi(\cdot)$  variations to event reconstruction in future publications.

## 3 Algorithms and their performance

Waveform analysis is to obtain  $t_i$  and  $q_i$  estimators  $\hat{t}_i$  and  $\hat{q}_i$  from waveform  $w(t)$ , where the output indices  $i$  are from 1 to  $\hat{N}_{\text{PE}}$  and  $\hat{N}_{\text{PE}}$  is an estimator of  $N_{\text{PE}}$  in eq. (4). Figure 2b illustrates the input waveform  $w(t)$  and the outputs charge  $\hat{\mathbf{t}}, \hat{\mathbf{q}}$  obtained from  $w(t)$ , where boldface  $\hat{\mathbf{t}}$  denotes the vector  $\hat{t}_i$ .

$\hat{N}_{\text{PE}}$  fails to estimate  $N_{\text{PE}}$  due to the fluctuation of  $q_i$  and the ambiguity of  $\hat{t}_i$ . For example, 1, 2 and even 3 PEs can generate the same charge as 1.6 units. A single PE charged 1 might be misinterpreted as 2 PEs at consecutive  $\hat{t}_i$  and  $\hat{t}_{i+1}$  with  $\hat{q}_i = \hat{q}_{i+1} = 0.5$ .

### 3.1 Evaluation criteria

Subject to such ambiguity of  $t_i/q_i$ , we introduce a set of evaluation criteria to assess the algorithms' performance.

### 3.1.1 Kullback-Leibler divergence

We construct a light curve estimator  $\hat{\phi}(t)$  from  $\hat{\mathbf{t}}$ ,  $\hat{\mathbf{q}}$  and  $\hat{N}_{\text{PE}}$ ,

$$\hat{\phi}(t) = \sum_{i=1}^{\hat{N}_{\text{PE}}} \hat{q}_i \delta(t - \hat{t}_i), \quad (9)$$

which resembles eq. (4). Consider the non-normalized Kullback-Leibler (KL) divergence [12] between  $\hat{\phi}(t)$  and  $\mu\phi(t - t_0)$ ,

$$\begin{aligned} D_{\text{KL}} \left[ \hat{\phi}(t) \parallel \mu\phi(t - t_0) \right] &= \int \left[ \hat{\phi}(t) \log \frac{\hat{\phi}(t)}{\mu\phi(t - t_0)} + \mu\phi(t - t_0) - \hat{\phi}(t) \right] dt \\ &= - \int \hat{\phi}(t) \log \phi(t - t_0) dt - \log \mu \int \hat{\phi}(t) dt + \mu + \int \left[ \hat{\phi}(t) \log \hat{\phi}(t) - \hat{\phi}(t) \right] dt \\ &= - \sum_{i=1}^{\hat{N}_{\text{PE}}} \int \hat{q}_i \delta(t - \hat{t}_i) \log \phi(t - t_0) dt - \log \mu \int \hat{q}_i \delta(t - \hat{t}_i) dt + \mu + C \\ &= - \log \prod_{i=1}^{\hat{N}_{\text{PE}}} [\phi(\hat{t}_i - t_0)]^{\hat{q}_i} - \log \mu \sum_{i=1}^{\hat{N}_{\text{PE}}} \hat{q}_i + \mu + C \end{aligned} \quad (10)$$

where  $C$  is a constant regarding  $t_0$  and  $\mu$ . Define the time KL estimator as

$$\begin{aligned} \hat{t}_{\text{KL}} &= \arg \min_{t_0} D_{\text{KL}} \left[ \hat{\phi}(t) \parallel \mu\phi(t - t_0) \right] \\ &= \arg \max_{t_0} \prod_{i=1}^{\hat{N}_{\text{PE}}} [\phi(\hat{t}_i - t_0)]^{\hat{q}_i}, \end{aligned} \quad (11)$$

which reduces to an MLE like eq. (6) if  $\hat{q}_i \equiv 1$ .  $\hat{t}_{\text{KL}}$  estimates  $t_0$  when  $t_i, q_i, N_{\text{PE}}$  are all uncertain. Denoting  $\Delta t_0$  as  $\hat{t}_{\text{KL}} - t_0$ , the standard deviation  $\sigma_{\text{KL}}$  of  $\Delta t_0$  on a batch of waveforms is the resolution of an algorithm.

The intensity KL estimator is,

$$\hat{\mu}_{\text{KL}} = \arg \min_{\mu} D_{\text{KL}} \left[ \hat{\phi}(t) \parallel \mu\phi(t - t_0) \right] = \sum_{i=1}^{\hat{N}_{\text{PE}}} \hat{q}_i. \quad (12)$$

### 3.1.2 Residual sum of squares

Following eqs. (5) and (9), we construct an estimator of a waveform,

$$\hat{w}(t) = \sum_{i=1}^{\hat{N}_{\text{PE}}} \hat{q}_i V_{\text{PE}}(t - \hat{t}_i) = \hat{\phi}(t) \otimes V_{\text{PE}}(t). \quad (13)$$

For a noise-free evaluation of  $\hat{w}(t)$ , residual sum of squares (RSS) is a  $\ell_2$ -distance of it to  $\tilde{w}(t)$ ,

$$\text{RSS} := \int [\hat{w}(t) - \tilde{w}(t)]^2 dt. \quad (14)$$

Figure 4 demonstrates that if two functions do not overlap, their RSS remain constant regardless of relative positions. The delta functions in the sampled light curves  $\hat{\phi}(t)$  and  $\tilde{\phi}(t)$  hardly overlap, rendering RSS useless. Furthermore, RSS cannot compare a discrete function with a continuous one. We shall only consider the RSS of waveforms.

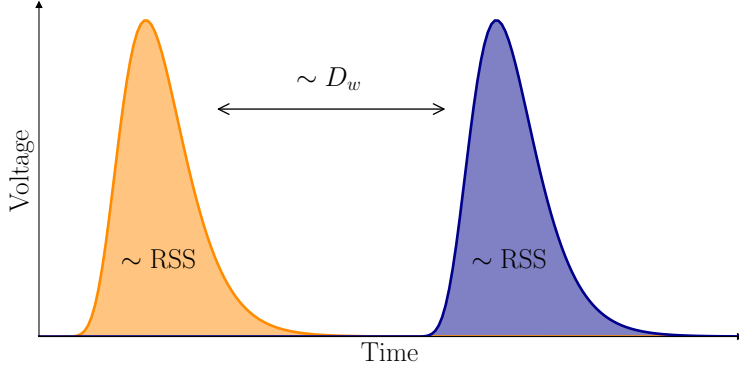


Figure 4: The RSS of red and blue curves is a function of the two shaded regions. It is a constant when the curves shift horizontally when they do not overlap. In contrast, the Wasserstein distance  $D_w$  of the two curves is associated with their separation. It complements RSS and offers a time-sensitive metric suitable for the sparse PE space.

### 3.1.3 Wasserstein distance

Wasserstein distance  $D_w$  is a metric between two distributions, either of which can be discrete or continuous. It can capture the difference between a waveform analysis result  $\hat{\phi}$  and the sampled light curve  $\tilde{\phi}(t)$  in eq. (4).

$$D_w [\hat{\phi}_*, \tilde{\phi}_*] = \inf_{\gamma \in \Gamma} \left[ \int |t_1 - t_2| \gamma(t_1, t_2) dt_1 dt_2 \right], \quad (15)$$

where  $*$  denotes the normalized light curves and  $\Gamma$  is the collection of joint distributions with marginals  $\hat{\phi}_*(t)$  and  $\tilde{\phi}_*(t)$ ,

$$\Gamma = \left\{ \gamma(t_1, t_2) \mid \int \gamma(t_1, t_2) dt_1 = \tilde{\phi}_*(t_2), \int \gamma(t_1, t_2) dt_2 = \hat{\phi}_*(t_1) \right\}.$$

It is also known as the *earth mover's distance* [13], encoding the minimum cost to transport mass from one distribution to another in figure 4.

Alternatively, we can calculate  $D_w$  from cumulative distribution functions (CDF). Let  $\hat{\Phi}(t)$  and  $\tilde{\Phi}(t)$  denote the CDF of  $\hat{\phi}_*(t)$  and  $\tilde{\phi}_*(t)$ , respectively. Then  $D_w$  is equivalent to the  $\ell_1$ -metric between the two CDFs,

$$D_w [\hat{\phi}_*, \tilde{\phi}_*] = \int |\hat{\Phi}(t) - \tilde{\Phi}(t)| dt. \quad (16)$$

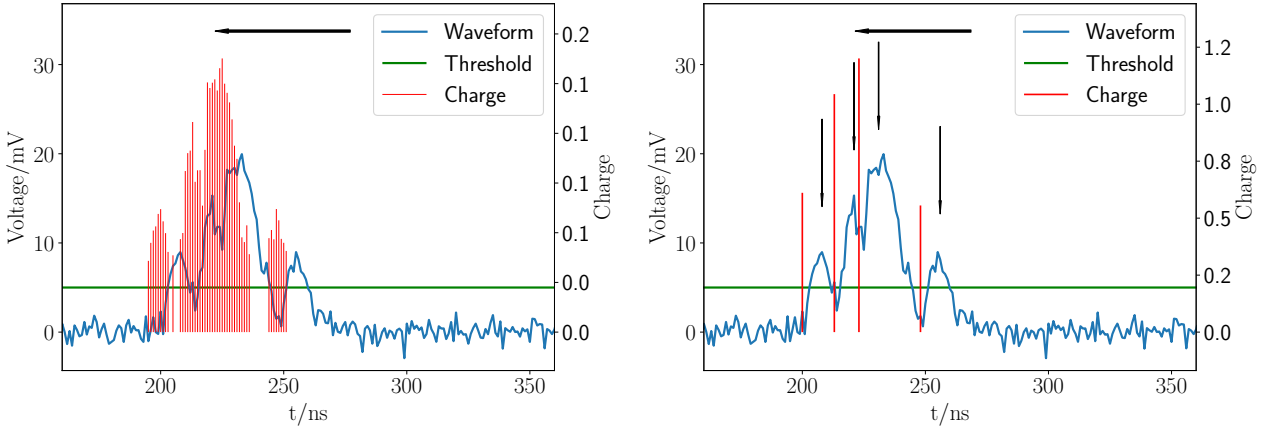
In the following, we evaluate the performance of waveform analysis algorithms ranging from heuristics, deconvolution, neural network to regression by the criteria discussed in this section.

## 3.2 Heuristic methods

By directly extracting waveform features, heuristic methods are straightforward and widely used.

### 3.2.1 Waveform shifting

By *waveform shifting*, we extract more time information than TDC: select all the  $t_i$  where the waveform  $w(t_i)$  exceeds a threshold to suppress noise, shift them by  $\Delta t$  according to the shape of the single PE response  $V_{\text{PE}}(t)$  in eq. (3) to get  $\hat{t}_i$ , then take  $\hat{q}_i \propto w(\hat{t}_i - \Delta t)$  so that the RSS is minimized. Though the obtained  $\hat{q}_i$ 's are smaller than PE charges as in figure 5a, waveform shifting does minimal analysis and serves as a baseline method.



(a) A waveform shifting example gives  
 $\Delta t_0 = -0.69 \text{ ns}$ , RSS = 369.6 mV<sup>2</sup>,  $D_w = 3.11 \text{ ns}$ .

(b) A peak finding example gives  
 $\Delta t_0 = -1.93 \text{ ns}$ , RSS = 266.9 mV<sup>2</sup>,  $D_w = 2.40 \text{ ns}$ .

Figure 5: Demonstrations of heuristic methods on a waveform sampled from  $\mu = 4$ ,  $\tau_\ell = 20 \text{ ns}$ ,  $\sigma_\ell = 5 \text{ ns}$  light curve conditions. Peak finding in (b) handles charges more realistically than waveform shifting in (a), giving better numbers by the RSS and  $D_w$  criteria in section 3.1.

### 3.2.2 Peak finding

*Peak finding* is more effective than waveform shifting by exploiting PE pulses. We smooth the waveforms by a low-pass Savitzky-Golay filter [14] and find all the peaks at  $t_i$ . The following resembles waveform shifting: apply a shift  $\Delta t$  to get  $\hat{t}_i$ , take  $\hat{q}_i \propto w(\hat{t}_i - \Delta t)$  to minimize the RSS. As shown in figure 5b, peak finding outputs charges close to 1 and works well for lower PE counts. But when PEs pile up closely, peaks overlap intensively, making this method unreliable.

## 3.3 Deconvolution

Deconvolution methods contribute more than heuristic ones by using the entire shape of  $V_{\text{PE}}(t)$ , thus can accommodate overshoots and pile-ups. Smoothing is necessary since deconvolution does not model the white noise.

### 3.3.1 Fourier deconvolution

*Fourier deconvolution* is an option considered by JUNO prototype [8]. The deconvolution relation is evident in the Fourier transform  $\mathcal{F}$  to eq. (5),

$$\mathcal{F}[w] = \mathcal{F}[\tilde{\phi}] \mathcal{F}[V_{\text{PE}}] + \mathcal{F}[\epsilon] \implies \mathcal{F}[\tilde{\phi}] = \frac{\mathcal{F}[w]}{\mathcal{F}[V_{\text{PE}}]} - \frac{\mathcal{F}[\epsilon]}{\mathcal{F}[V_{\text{PE}}]}. \quad (17)$$

By low-pass filtering the waveform  $w(t)$  to get  $\hat{w}(t)$ , we suppress the noise term  $\epsilon$ , take the inverse Fourier transform  $\hat{\phi}_1(t) = \mathcal{F}^{-1} \left[ \frac{\mathcal{F}[\hat{w}]}{\mathcal{F}[V_{\text{PE}}]} \right](t)$ , and compute  $\hat{\phi}(t)$  as the over-threshold  $q_{\text{th}}$  part of  $\hat{\phi}_1(t)$ ,

$$\hat{\phi}(t) = \hat{\alpha} \underbrace{\hat{\phi}_1(t) I(\hat{\phi}_1(t) - q_{\text{th}})}_{\text{over-threshold part of } \hat{\phi}_1(t)} \quad (18)$$

where  $I(x)$  is the indicator function, and  $\hat{\alpha}$  is a scaling factor to minimize RSS,

$$I(x) = \begin{cases} 1 & , \text{if } x \geq 0, \\ 0 & , \text{otherwise} \end{cases} \quad \hat{\alpha} = \arg \min_{\alpha} \text{RSS} [\alpha \hat{w}(t), w(t)].$$

$\tilde{w}(t)$  unknown in data analysis, we replace it in eq. (14) with  $w(t)$ .

Figure 6a illustrates that Fourier deconvolution outperforms heuristic methods. Meanwhile, noise and precision loss in the waveform lead to smaller and even negative  $\hat{q}_i$ . Those can be mitigated by thresholding and scaling in eq. (18), but call for a more elegant solution.

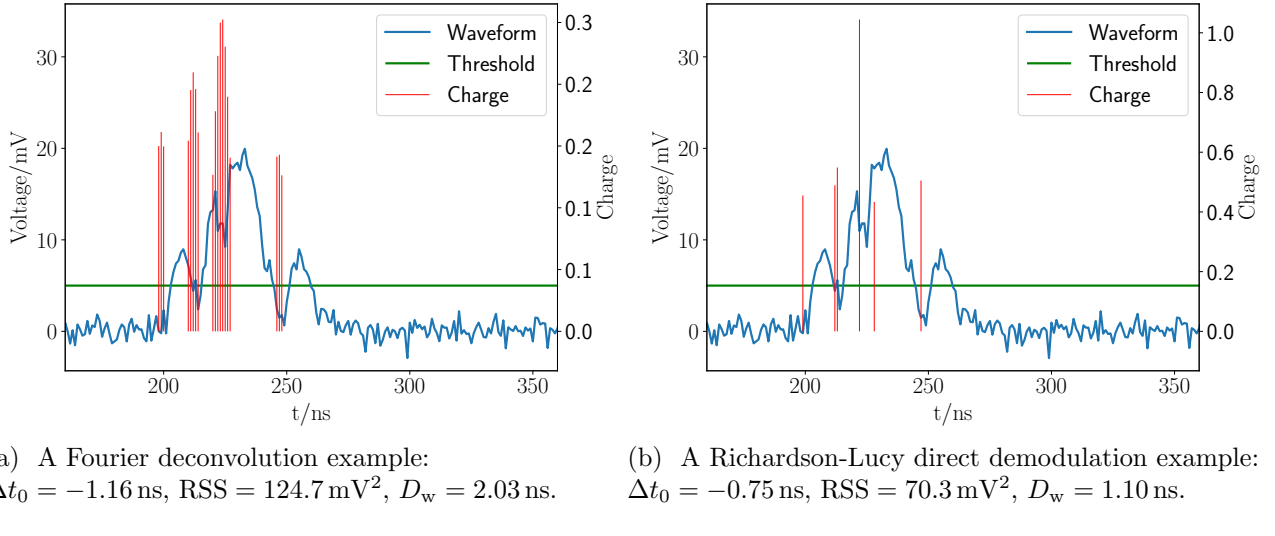


Figure 6: Demonstrations of deconvolution methods on a waveform sampled from the same setup as figure 5. Richardson-Lucy direct demodulation in (b) imposes positive charges in iterations and obtains better results than Fourier deconvolution in (a).

### 3.3.2 Richardson-Lucy direct demodulation

*Richardson-Lucy direct demodulation* (LucyDDM) [15] with a non-linear iteration to calculate deconvolution has a wide application in astronomy [16] and image processing. We view  $V_{\text{PE}*}(t-s)$  as a conditional probability distribution  $p(t|s)$  where  $t$  denotes PMT amplified electron time, and  $s$  represents the given PE time. By the Bayesian rule,

$$\tilde{\phi}_*(s)V_{\text{PE}*}(t-s) = \tilde{\phi}_*(s)p(t|s) = p(t,s) = \tilde{w}_*(t)p(s|t), \quad (19)$$

where  $p(t,s)$  is the joint distribution of amplified electron  $t$  and PE time  $s$ , and  $\tilde{w}$  is the smoothed  $w$ . Cancel out the normalization factors,

$$p(s|t) = \frac{\tilde{\phi}_*(s)V_{\text{PE}*}(t-s)}{\tilde{w}_*(t)} = \frac{\tilde{\phi}(s)V_{\text{PE}}(t-s)}{\int \tilde{\phi}(s')V_{\text{PE}}(t-s')ds'}. \quad (20)$$

Then a recurrence relation  $\phi_*$  is,

$$\begin{aligned} \tilde{\phi}_*(s) &= \int p(s|t)\tilde{w}_*(t)dt = \int \frac{\tilde{\phi}(s)V_{\text{PE}}(t-s)}{\int \tilde{\phi}(s')V_{\text{PE}}(t-s')ds'}\tilde{w}_*(t)dt \\ \implies \hat{\phi}^{n+1}(s) &= \int \frac{\hat{\phi}^n(s)V_{\text{PE}*}(t-s)}{\int \hat{\phi}^n(s')V_{\text{PE}}(t-s')ds'}\tilde{w}(t)dt, \end{aligned} \quad (21)$$

where only  $V_{\text{PE}*}$  in the numerator is normalized, and superscript  $n$  denotes the iteration step. Like Fourier deconvolution in eq. (18), we threshold and scale the converged  $\hat{\phi}^\infty$  to get  $\hat{\phi}$ . As shown in figure 6b, the positive constraint of  $\hat{\phi}$  makes LucyDDM more resilient to noise.

The remaining noise in the smoothed  $\tilde{w}$  crucially influences deconvolution. A probabilistic method will correctly model the noise term  $\epsilon$ , as we shall see in section 3.5. Before that, let us try something different.

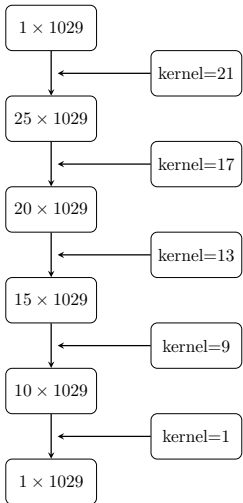
### 3.4 Convolutional neural network

Convolutional neural networks (CNN) made breakthroughs in various fields like computer vision [17] and natural language processing [18]. As an efficient composition of weighted additions and non-linear functions, neural networks outperform many traditional algorithms.

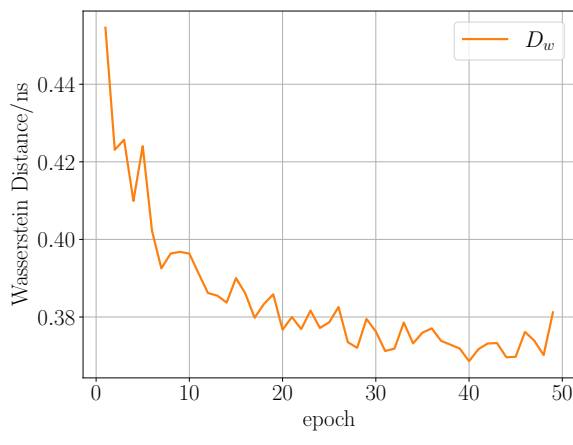
We choose a shallow network structure of 5 layers to recognize patterns as shown in figure 7a, motivated by the pulse shape and universality of  $V_{\text{PE}}(t)$  for all the PEs. The convolutional widths are selected considering the localized nature of  $V_{\text{PE}}(t)$ .

The workflow of data processing consists of training and predicting. We find a mapping from waveform  $w(t)$  to PE  $\phi(t)$  with the backpropagation method and supervised learning. We formulate the training loss as optimizing  $D_w[\phi, \tilde{\phi}]$ , the Wasserstein distance between the truth  $\phi$  and predicted  $\tilde{\phi}$ . As discussed in section 3.1.3,  $D_w$  can handle the PE sparsity in training iterations. Figure 7b shows the convergence of Wasserstein distance during training.

The output of CNN is scaled by  $\hat{\alpha}$  following eq. (18) to get  $\hat{\phi}$ .



(a) Structure of the neural network.

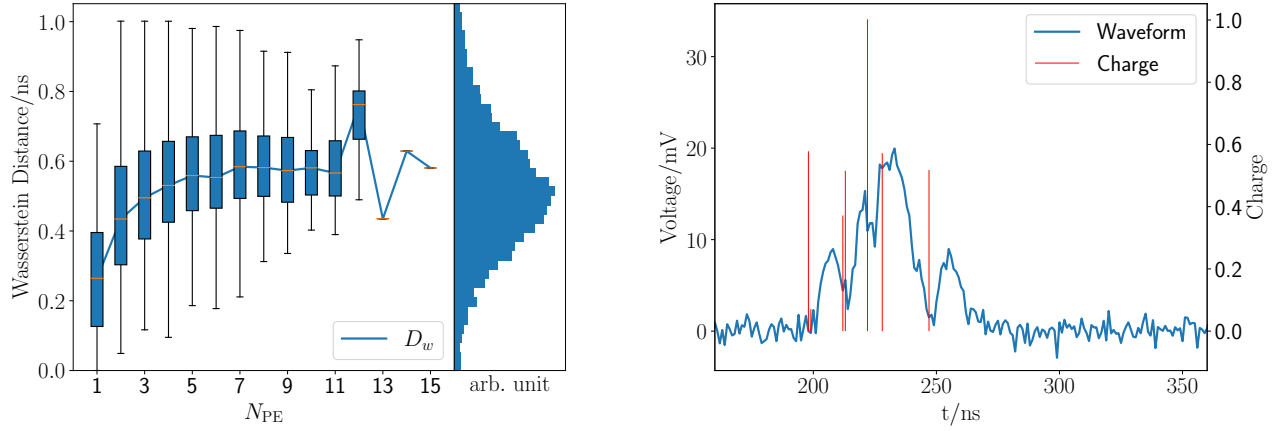


(b) Evolution of loss.

Figure 7: Training process of a CNN. A shallow network structure of 5 layers in (a) is trained to converge in Wasserstein distance as shown in (b). “kernel=21” stands for a 1 dimensional convolutional kernel of length 21. “1029” is the number of voltage samples in a waveform.  $1 \times$  represents the number of channels in each layer.

In figure 8a, we use box-plots to describe  $D_w$  distributions. In figure 8a,  $D_w$  is the smallest for one PE.  $D_w$  stops increasing with  $N_{\text{PE}}$  at about 6 PEs, where the PE times are the most challenging to extract. When  $N_{\text{PE}}$  is more than 6, pile-ups tend to produce a continuous waveform and the average PE time accuracy stays flat. Thus waveform analysis is the most important in recovering time accuracy for PEs less than 10.

Such small  $D_w$  in figure 8a provides a precise matching of waveforms horizontally to guarantee effective  $\hat{\alpha}$  scaling, explaining why RSS is also small in figure 8b.



(a)  $D_w$  histogram and its distributions conditioned on  $N_{\text{PE}}$ . “arbi. unit” means arbitrary unit.

(b) An example giving  $\Delta t_0 = -3.05 \text{ ns}$ ,  $\text{RSS} = 10.0 \text{ mV}^2$ ,  $D_w = 0.64 \text{ ns}$ .

Figure 8: Demonstration of CNN on  $10^4$  waveforms in (a) and one waveform in (b) sampled from the same setup as figure 5. In figure (a), the middle line is the median of the distribution. The upper and lower hinges are the first percentile  $Q_1$  at 25 % and the third percentile  $Q_3$  at 75 %. The upper and lower whiskers are  $Q_1 \pm 1.5(Q_3 - Q_1)$ .

### 3.5 Regression analysis

With the generative waveform model in eq. (5), regression is ideal for analysis. Although computational complexity hinders the applications of regression by the vast volumes of raw data, the advancement of sparse models and big data infrastructures strengthens the advantage of regression.

We replace  $\hat{N}_{\text{PE}}$  with a fixed sample size  $N_s$  and  $\hat{t}_i$  with a fixed grid of times  $t'_i$  in eq. (13),

$$w'(t) = \sum_{i=1}^{N_s} q'_i V_{\text{PE}}(t - t'_i). \quad (22)$$

When  $\{t'_i\}$  is dense enough,  $\{\hat{q}_i\}$  determines the inferred PE distribution  $\hat{\phi}(t)$ ,

$$\hat{\phi}(t) = \sum_{i=1}^{N_s} \hat{q}_i \delta(t - t'_i). \quad (23)$$

From the output  $\hat{\phi}_{\text{dec}}(t)$  of a deconvolution method in section 3.3.2, we confidently leave out all the  $t'_i$  that  $\hat{\phi}_{\text{dec}}(t'_i) = 0$  in eq. (23) to reduce the number of parameters and the complexity.

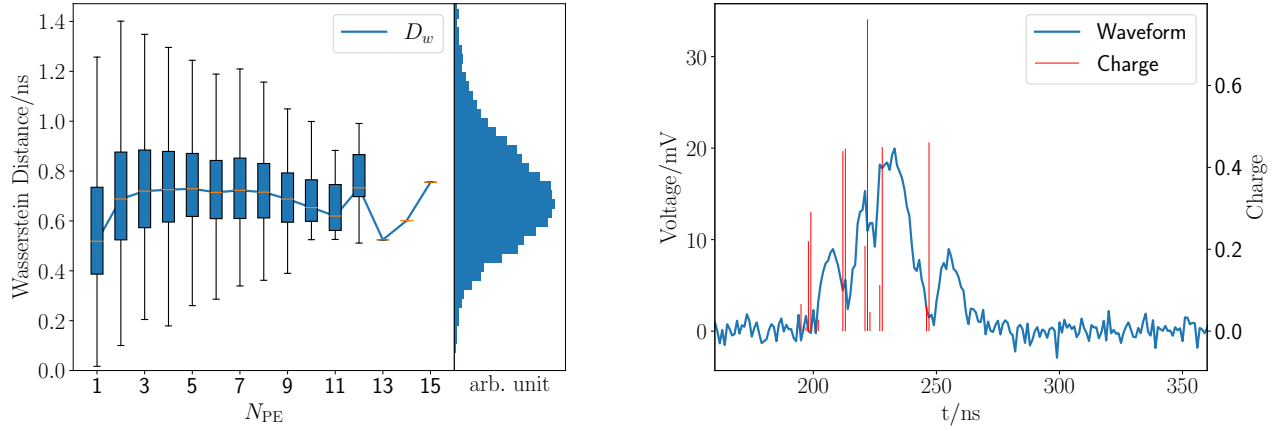
We attempted to replace the dense  $\mathbf{t}'$  grid in eq. (22) with a length-varying vector of sparse PEs. However, the truth  $N_{\text{PE}}$  is unknown and formulating an explicit trans-dimensional model is expansive. We shall leave it to section 3.5.3.

#### 3.5.1 Direct charge fitting

Fitting the charges  $q'_i$  in eq. (22) directly by minimizing RSS of  $w'(t)$  and  $w(t)$ , we get

$$\hat{\mathbf{q}} = \arg \min_{q'_i \geq 0} \text{RSS} [w'(t), w(t)]. \quad (24)$$

Slawski and Hein [19] prove that in deconvolution problems, the non-negative least-squares formulation in eq. (24) is self-regularized and gives sparse solutions of  $q'_i$ . We optimize eq. (24) by Broyden-Fletcher-Goldfarb-Shanno algorithm with a bound constraint [20]. In figure 9a, charge fitting is consistent in  $D_w$  for different  $N_{\text{PE}}$ 's, showing its resilience to pile-up.



(a)  $D_w$  histogram and its distributions conditioned on  $N_{PE}$ , box-plot explained in figure 8.

(b) An example giving  $\Delta t_0 = -3.23$  ns,  $RSS = 7.64$  mV $^2$ ,  $D_w = 0.68$  ns.

Figure 9: Demonstration of direct charge fitting with  $10^4$  waveforms in (a) and one waveform in (b) sampled from the same setup as figure 5. Direct charge fitting shows a better performance than LucyDDM in figure 6b and a comparable  $D_w$  to CNN in figure 8b.

The sparsity of  $q'_i$  is evident in figure 9b. However, the majority of the  $\hat{q}_i$  are less than 1. This feature motivates us to incorporate prior knowledge of  $q'_i$  towards a more dedicated model than directly fitting charges.

### 3.5.2 Markov chain Monte Carlo

Chaining the  $q'_i$  distribution (section 2.2), the charge fitting eq. (24) and the light curve eq. (2), we arrive at a hierarchical Bayesian model,

$$\begin{aligned}
 t_0 &\sim \mathcal{U}(0, \bar{t}_0) \\
 \mu_i &= \mu \int_{t'_i - \frac{\Delta t'}{2}}^{t'_i + \frac{\Delta t'}{2}} \phi(t' - t_0) dt' \approx \mu \phi(t'_i - t_0) \Delta t' \\
 z_i &\sim \mathcal{B}(\mu_i) \\
 q'_{i,0} &= 0 \\
 q'_{i,1} &\sim \mathcal{N}(1, \sigma_q^2) \\
 q'_i &= q'_{i,z_i} \\
 w'(t) &= \sum_{i=1}^{N_s} q'_i V_{PE}(t - t'_i) \\
 w(t) &\sim \mathcal{N}(w'(t), \sigma_\epsilon^2)
 \end{aligned} \tag{25}$$

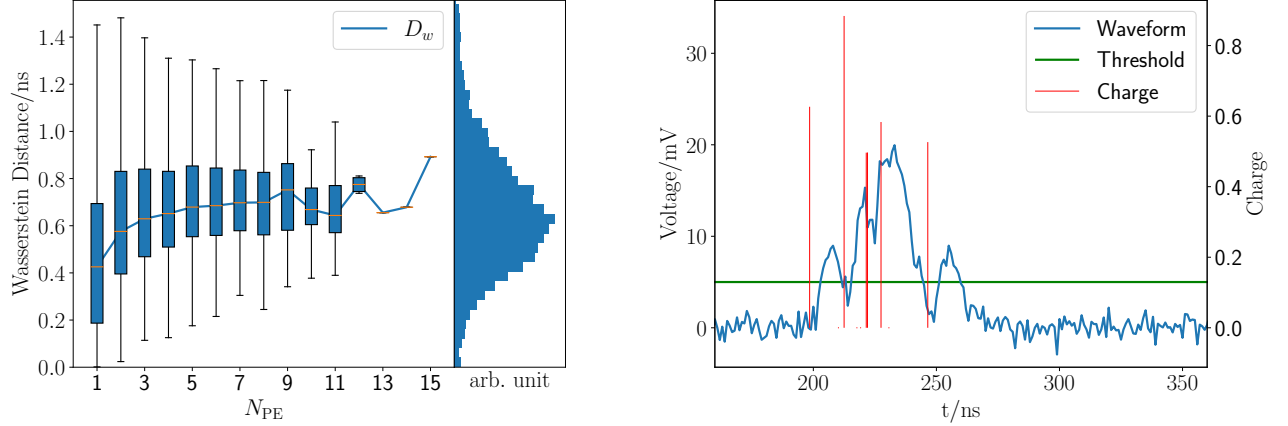
where  $\mathcal{U}$  and  $\mathcal{B}$  stand for uniform and Bernoulli distributions,  $\bar{t}_0$  is an upper bound of  $t_0$ , and  $q'_i$  is a mixture of 0 (no PE) and normally distributed  $q'_{i,1}$  (1 PE). When the expectation  $\mu_i$  of a PE hitting  $(t'_i - \frac{\Delta t'}{2}, t'_i + \frac{\Delta t'}{2})$  is small enough, that 0-1 approximation is valid. The inferred waveform  $w'(t)$  differs from observable  $w(t)$  by a white noise  $\epsilon(t) \sim \mathcal{N}(0, \sigma_\epsilon^2)$  motivated by eq. (5). When an indicator  $z_i = 0$ , it turns off  $q'_i$ , reducing the number of parameters by one. That is how eq. (25) achieves sparsity.

We generate posterior samples of  $t_0$  and  $\mathbf{q}'$  by Hamiltonian Monte Carlo (HMC) [21], a variant of Markov chain Monte Carlo suitable for high-dimensional problems. Construct  $\hat{t}$  and  $\hat{q}_i$  as the mean estimators of posterior samples  $t_0$  and  $q'_i$  at  $z_i = 1$ . Unlike the  $\hat{t}_{KL}$  discussed in section 3.1.1,  $\hat{t}_0$  is a

direct Bayesian estimator from eq. (25). We construct  $\hat{\phi}(t)$  by eq. (23) and  $\hat{w}(t)$  by

$$\hat{w}(t) = \sum_{i=1}^{N_s} \hat{q}_i V_{\text{PE}}(t - t'_i). \quad (26)$$

RSS and  $D_w$  are then calculated according to eqs. (14) and (16).



(a)  $D_w$  histogram and its distributions conditioned on  $N_{\text{PE}}$ , box-plot explained in figure 8.

(b) An example with  $\Delta t_0 = -2.48 \text{ ns}$ ,  $\text{RSS} = 16.25 \text{ mV}^2$ ,  $D_w = 0.76 \text{ ns}$ .

Figure 10: Demonstration of MCMC with  $10^4$  waveforms in (a) and one waveform in (b) sampled from the same setup as figure 5. Although using a more dedicated model, MCMC performs worse than the direct charge fitting in figure 9. We suspect the Markov chain is not long enough.

Although we imposed a  $\mathcal{N}(1, \sigma_q^2)$  prior, The charges  $\hat{q}_i$  in figure 9b are still less than 1. The  $D_w$  marginal distribution in figure 10a is less smooth than that of the direct charge fitting in figure 9a. Similarly, RSS in figure 10b is slightly worse than that in figure 9b. We suspect the Markov chain has not finally converged due to the trans-dimensional property of eq. (25). Extending the chain is not a solution because MCMC is already much slower than direct fitting in section 3.5.1. We need an algorithm that pertains to the model of eq. (25) but much faster than MCMC.

### 3.5.3 Fast stochastic matching pursuit

In reality,  $w(t)$  is discretized as  $\mathbf{w}$ . If we rewrite the hierarchical model (25) into a joint distribution, marginalizing out  $\mathbf{q}'$  and  $\mathbf{z}$  gives a flattened model,

$$\begin{aligned} p(\mathbf{w}, t_0, \mu) &= \sum_{\mathbf{z}} \int d\mathbf{q}' p(\mathbf{w}, \mathbf{q}', \mathbf{z}, t_0, \mu) \\ &= p(t_0, \mu) \sum_{\mathbf{z}} \left[ \int d\mathbf{q}' p(\mathbf{w}|\mathbf{q}') p(\mathbf{q}'|\mathbf{z}) \right] p(\mathbf{z}|t_0, \mu) \\ &= p(t_0, \mu) \sum_{\mathbf{z}} p(\mathbf{w}|\mathbf{z}) p(\mathbf{z}|t_0, \mu) \\ &= p(t_0, \mu) p(\mathbf{w}|t_0, \mu) \end{aligned} \quad (27)$$

The integration over  $\mathbf{q}'$  is the probability density of a multi-normal distribution  $p(\mathbf{w}|\mathbf{z})$ , with a fast algorithm to iteratively compute by Schniter et al. [22]. The summation over  $\mathbf{z}$ , however, takes an exploding number of combinations.

Let's approximate the summation with a sample from  $S = (\mathbf{s}_1, \mathbf{s}_2, \dots, \mathbf{s}_M)$  by Metropolis-Hastings [23, 24, 25] from  $p(\mathbf{z}) = Cp(\mathbf{w}|\mathbf{z})h(\mathbf{z})$ .  $C$  is independent of  $\mathbf{z}$ , and  $h(\mathbf{z})$  is an educated guess for  $p(\mathbf{z}|t_0, \mu)$  from a previous method like LucyDDM (section 3.3.2). Then,

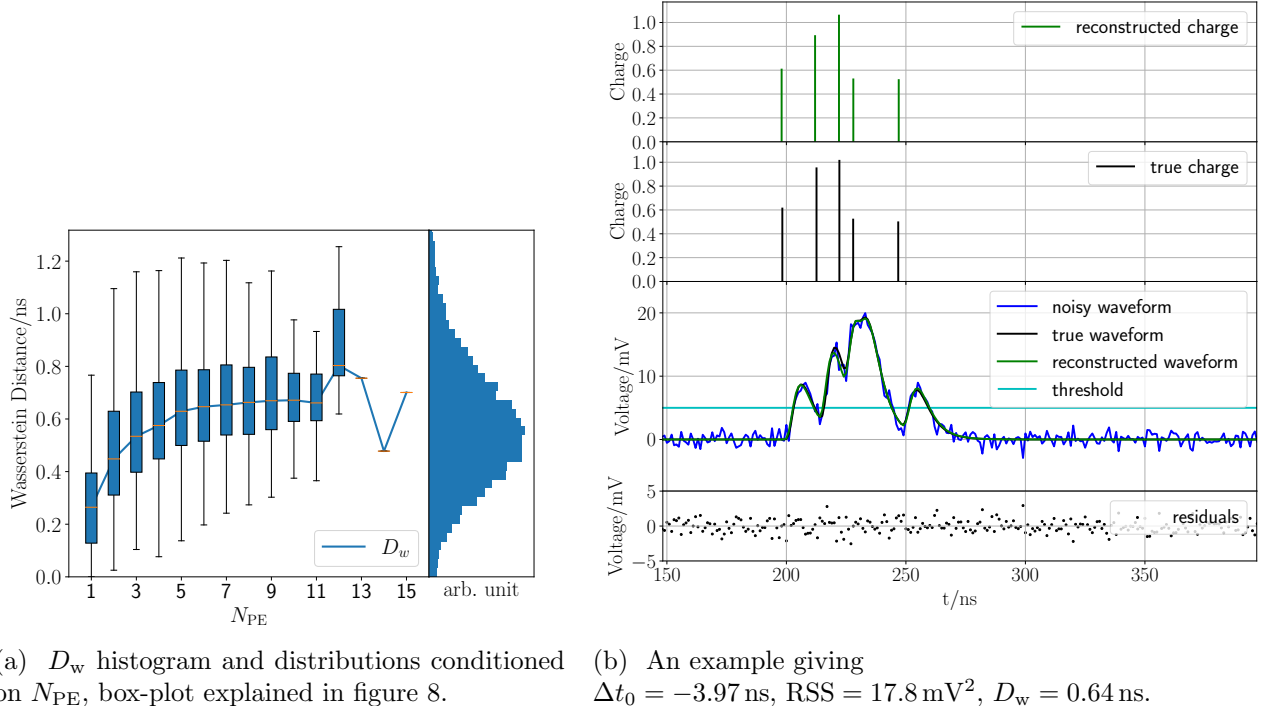
$$\begin{aligned} p(\mathbf{w}|\mu, t_0) &= \sum_{\mathbf{z}} p(\mathbf{w}|\mathbf{z})p(\mathbf{z}|t_0, \mu) = \frac{1}{C} \sum_{\mathbf{z}} p(\mathbf{z}) \frac{p(\mathbf{z}|\mu, t_0)}{h(\mathbf{z})} \\ &= \frac{1}{C} \mathbb{E}_{\mathbf{z}} \left[ \frac{p(\mathbf{z}|\mu, t_0)}{h(\mathbf{z})} \right] \approx \frac{1}{CM} \sum_{i=1}^M \frac{p(\mathbf{s}_i|\mu, t_0)}{h(\mathbf{s}_i)}. \end{aligned} \quad (28)$$

Construct approximate MLEs for  $t_0$ ,  $\mu$  and  $\mathbf{z}$ , and the expectation estimation of  $\hat{\mathbf{q}}$ ,

$$\begin{aligned} (\hat{t}_0, \hat{\mu}) &= \arg \max_{t_0, \mu} p(\mathbf{w}|\mu, t_0) = \arg \max_{t_0, \mu} \sum_{i=1}^M \frac{p(\mathbf{s}_i|\mu, t_0)}{h(\mathbf{s}_i)} \\ \hat{\mathbf{z}} &= \arg \max_{\mathbf{s}_i \in S} p(\mathbf{w}|\mathbf{s}_i)h(\mathbf{s}_i) \\ \hat{\mathbf{q}}|\hat{\mathbf{z}} &= \mathbb{E}(\mathbf{q}'|\mathbf{w}, \hat{\mathbf{z}}) \end{aligned} \quad (29)$$

RSS and  $D_w$  are calculated by eqs. (14), (16), (23) and (26).

We name the method *fast stochastic matching pursuit* (FSMP) after *fast Bayesian matching pursuit* (FBMP) by Schniter et al. [22] and *Bayesian stochastic matching pursuit* by Chen et al. [26]. Here FSMP replaces the greedy search routine in FBMP with stochastic sampling. With the help of Ekanadham et al.'s function interpolation [27], FSMP straightforwardly extends  $\mathbf{z}$  into an unbinned vector of PE locations  $t_i$ . Geyer and Møller [28] developed a similar sampler to handle trans-dimensionality in a Poisson point process.  $h(\mathbf{z})$  and the proposal distribution in Metropolis-Hastings steps could be tuned to improve sampling efficiency. We shall leave the detailed study of the Markov chain convergence to our future publications.



(a)  $D_w$  histogram and distributions conditioned on  $N_{PE}$ , box-plot explained in figure 8.

(b) An example giving  $\Delta t_0 = -3.97$  ns, RSS = 17.8 mV<sup>2</sup>,  $D_w = 0.64$  ns.

Figure 11: Demonstration of FSMP with  $10^4$  waveforms in (a) and one waveform in (b) sampled from the same setup as figure 5. FSMP reconstructs the waveform and charges flawlessly.

In terms of  $D_w$ , figure 11a shows that FSMP is on par with CNN in figure 8a. Figure 11b is a perfect reconstruction example where the true and reconstructed charges and waveforms overlap. A bias of  $\Delta t_0 = -3.97$  ns aligns with  $\hat{t}_{\text{ALL}}$  in eq. (6), which will be covered in section 4.3. The superior performance of FSMP attributes to sparsity and positiveness of  $q'_i$ , correct modeling of  $V_{\text{PE}}$ ,  $q'$  distribution and white noise.

Estimators for  $t_0$  and  $\mu$  in eq. (29) is an elegant interface to event reconstruction, eliminating the need of  $\hat{t}_{\text{KL}}$  and  $\hat{\mu}_{\text{KL}}$  in section 3.1.1.

## 4 Summary and discussion

This section will address the burning question: which waveform analysis method should my experiment use? We surveyed 8 methods, heuristics (figure 5), deconvolution (figure 6), neural network (figure 8) and regressions (figures 9–11), from the simplest to the most dedicated<sup>1</sup>. To make a choice, we shall investigate the light curve reconstruction precision under different light intensities  $\mu$ .

### 4.1 Performance

We constrain the candidates by time consumption, algorithm category and  $D_w$ . Figure 12 shows the  $D_w$  and time consumption summary of all eight methods with the same waveform sample as figure 5.

---

<sup>1</sup>The source codes are available on GitHub <https://github.com/heroxbd/waveform-analysis>.

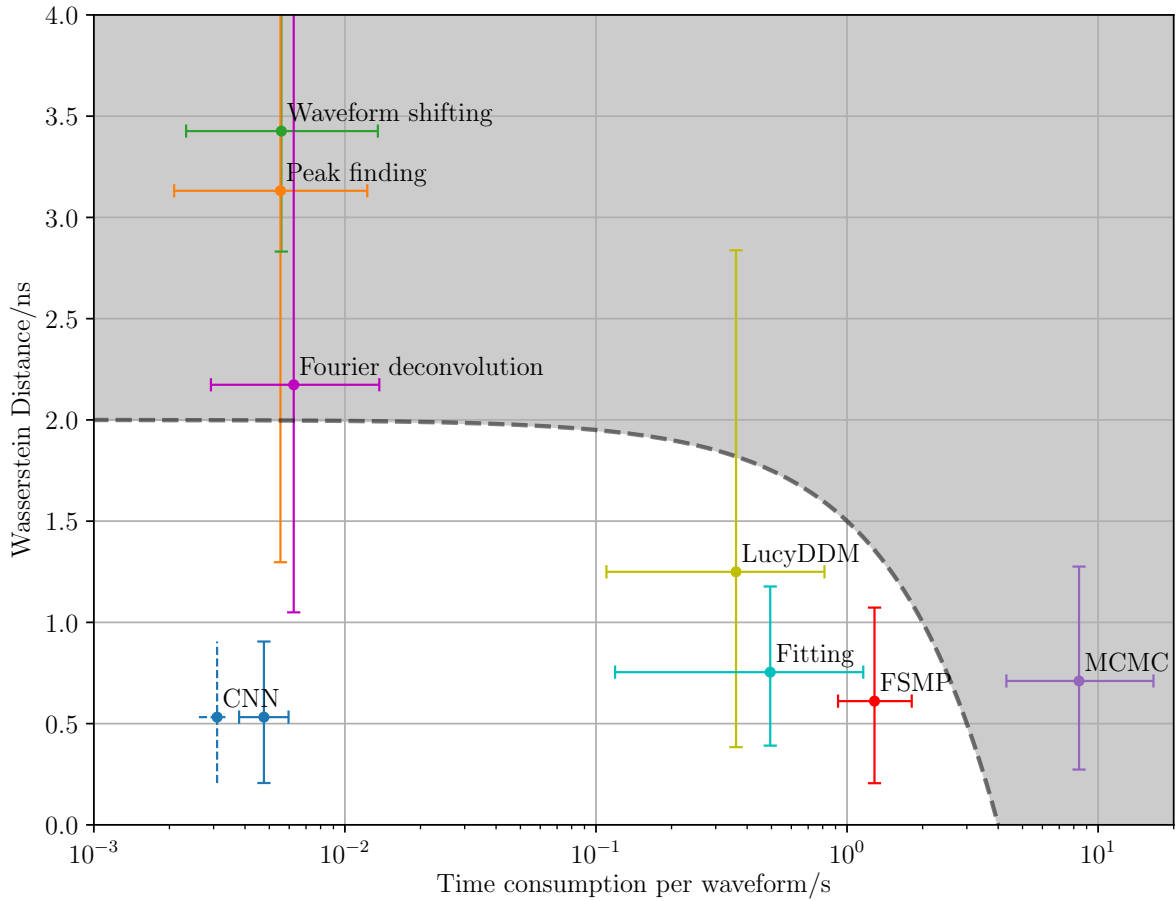


Figure 12: Performance of algorithms in terms of  $D_w$  and time consumption, evaluated on the same dataset as figure 5. Central points are the average results of  $10^4$  waveforms from specific  $\mu$  values. Error bars are 5–95 percentiles. Fitting stands for direct charge fitting. The time consumed by Fitting, MCMC and FSMP include the LucyDDM pre-conditioner’s initialization time. CNN’s time consumption is measured for inference in two conditions: GPU<sup>2</sup> (dashed error bars) and CPU<sup>3</sup> (solid error bars). Training a CNN is a one-time job, and its cost is not included in the plot.

The  $D_w$  performance of waveform shifting, peak finding and Fourier deconvolution are suboptimal. Like CNN, they are the fastest because no iteration is involved. LucyDDM and Fitting have  $\sim 100$  iterations, while FSMP has  $\sim 1000$  iterations, making them two orders of magnitudes slower. The number of iterations and samples  $N_s$  can be decreased to trade for speed. MCMC is too expensive and its principle is not too different from FSMP. We shall focus on CNN, LucyDDM, Fitting and FSMP in the following.

The  $D_w$  and RSS dependence on  $\mu$  of LucyDDM, Fitting, CNN and FSMP are plotted in figures 13a and 13b. When  $\mu$  increases the  $D_w$  of different methods approach each other, while the RSS diverges. Notice that in the qualitative discussion, large  $N_{PE}$ , large light intensity  $\mu$  and large pile-ups are used interchangeably. The  $D_w$  decrease-before-increase behavior is observed in section 3.4 that with large  $N_{PE}$  the overall PE times dominate. It is harder to be good at  $D_w$  and RSS with larger  $N_{PE}$ , but FSMP achieves the best balance. The Markov chains of FSMP have room for efficiency turning. Furthermore, implementing it in field-programmable gate array (FPGA) commonly found in front-end electronics will accelerate waveform analysis and reduce the volume of data acquisition. It is also interesting whether a neural network can approximate FSMP.

<sup>2</sup>Graphics card of NVIDIA® Tesla A100.

<sup>3</sup>One CPU core of AMD EYPC™ 7742.

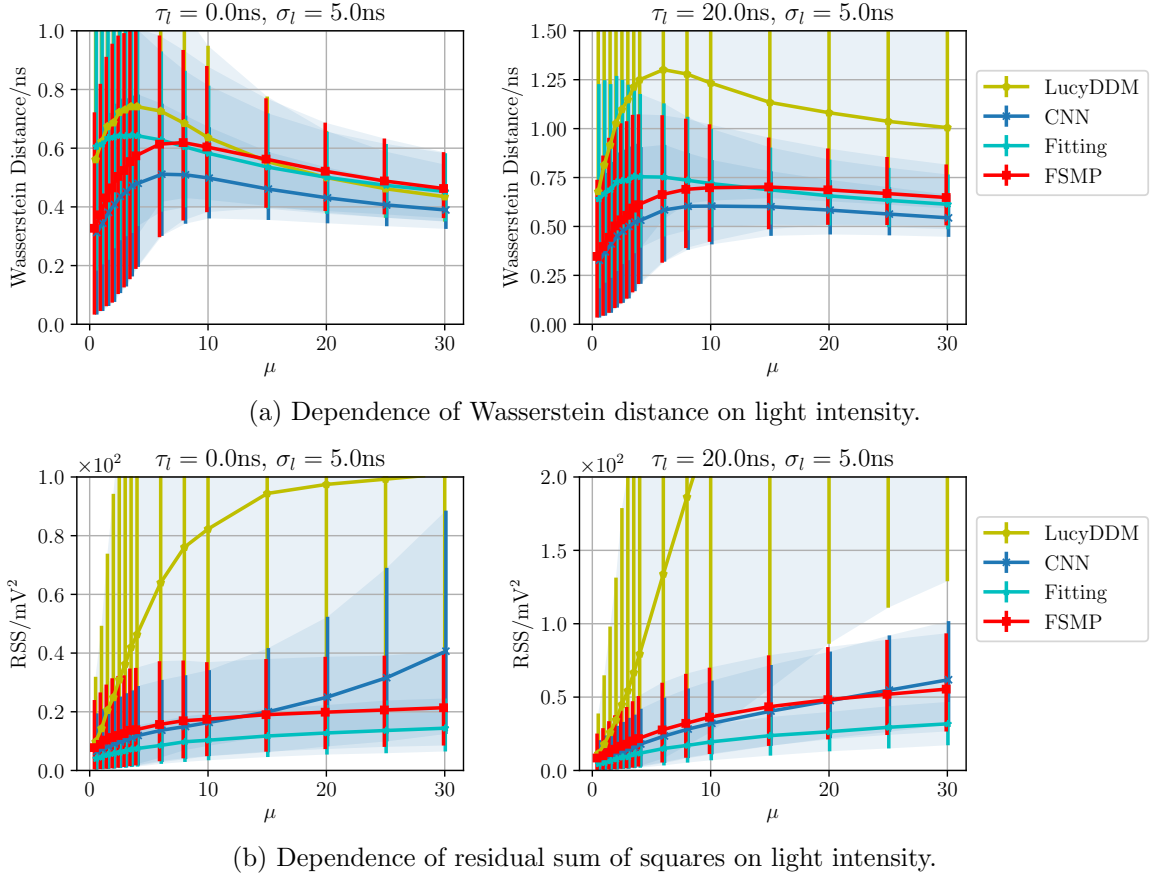


Figure 13: The dependence of  $D_w$  (a) and RSS (b) on light intensity  $\mu$  for typical Cherenkov (left) and scintillation (right) configurations. Central points, error bars and method abbreviations have the same meaning as figure 12. With more pile-ups,  $D_w$  tends to converge while RSS diverges. The pile-up effect is more significant for the Cherenkov case because the time scale of the light curve is narrower.

CNN and Fitting are the kings of  $D_w$  and RSS, because their loss functions are chosen accordingly. It is informative to study the posterior charge distribution that is not related to the loss function of any method.

## 4.2 Charge fidelity and sparsity

All the discussed methods output  $\hat{q}_i$  as the inferred charge of the PE at  $t'_i$ . Evident in figure 14, FSMP retains the true charge distribution. It is the only method modeling PE correctly.

In contrast, LucyDDM, Fitting and CNN distributions are severely distorted. During the optimization process of  $D_w$  or RSS,  $N_s$  (the number of  $q_i$ ) is a constant. Many  $\hat{q}_i$  are inferred to be fragmented values. Retaining charge distribution is a manifestation of sparsity. FSMP has the best sparsity because it chooses a PE configuration  $\mathbf{z}$  before fitting  $\hat{q}_i$ . CNN is somehow better than Fitting, although the latter in theory has self-regulated sparsity. It is interesting to notice, but the mechanism is unknown to us.

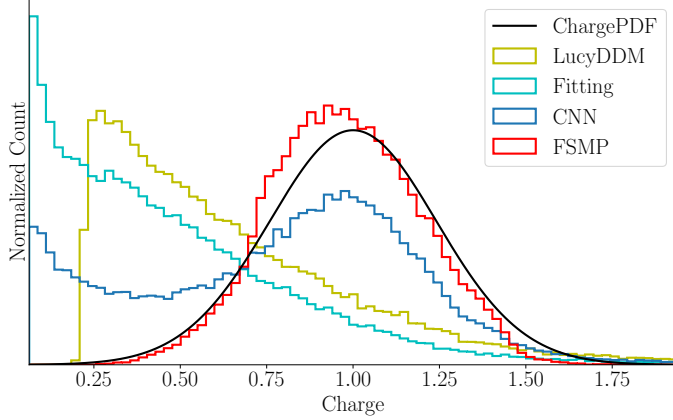


Figure 14:  $\hat{q}_i$  distributions on the same waveform dataset as figure 5. Method abbreviations are defined in figure 12. ‘‘ChargePDF’’ is the charge distribution of simulation input in section 2.2. The cut-off near 0 in LucyDDM is an artifact of thresholding in eq. (18).

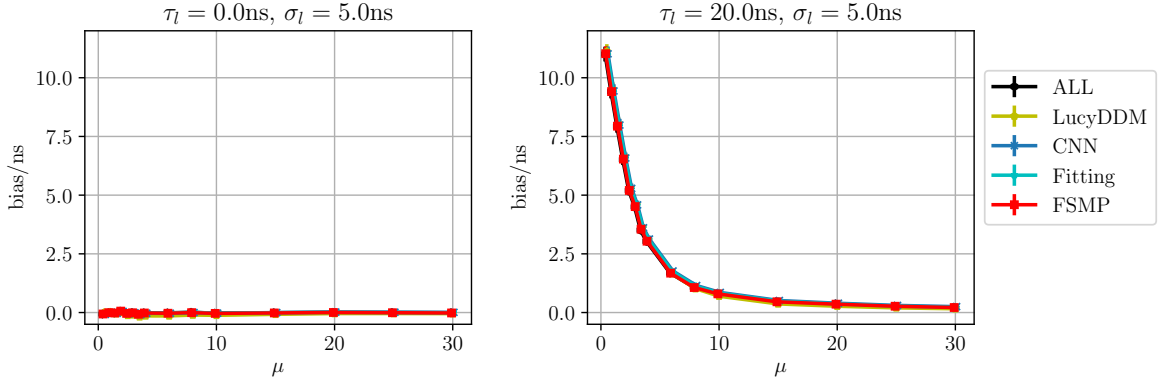
For large  $N_{\text{PE}}$ , the sparsity condition is by definition lost. The equivalence of charge fidelity and sparsity implies that FSMP performs similarly to others for these cases, as we shall see in the following sections.

### 4.3 Inference of incident light

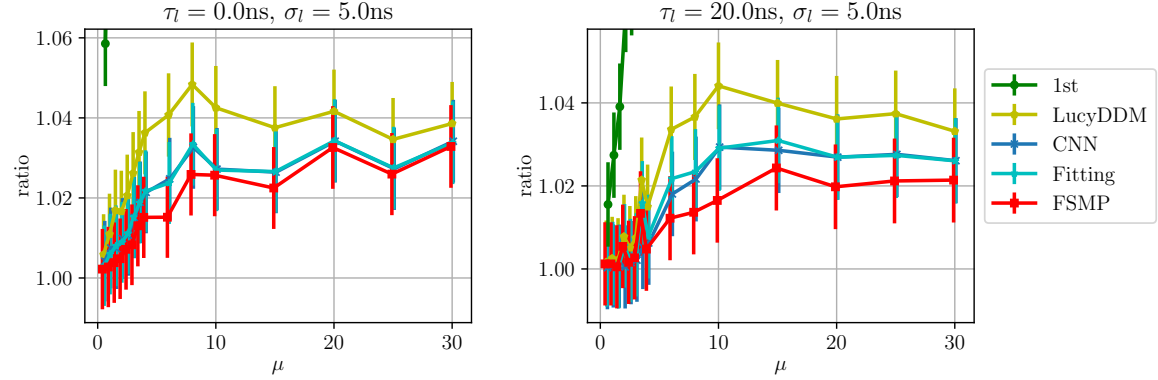
As figure 13, we show the dependence on  $\mu$  of bias (figure 15a) and resolution (figure 15b) for different time estimators in the two typical experimental setups. From figure 15a, we see that the  $t_0$  estimation biases are all similar to that of  $\hat{t}_{\text{ALL}}$ . The bias for the scintillation configuration (right of figure 15a) for small  $\mu$  is intrinsic for MLE of exponential distributions. We can modify it into an unbiased estimator, but leave this discussion to event reconstruction.

People often argue from difficulties for large pile-ups that waveform analysis is unnecessary. Comparing figures 3 and 15b, it is a myth. Although  $\hat{t}_{1\text{st}}$  is more precise for large light intensity, all the waveform analysis methods provide magnificently better time resolutions than  $\hat{t}_{1\text{st}}$ , more than twice for  $\mu > 20$  in Cherenkov setup. FSMP gives the most significant boost. Such improvement in time resolutions amounts to the position resolution, which benefits fiducial volume, exposure and position-dependent energy bias.

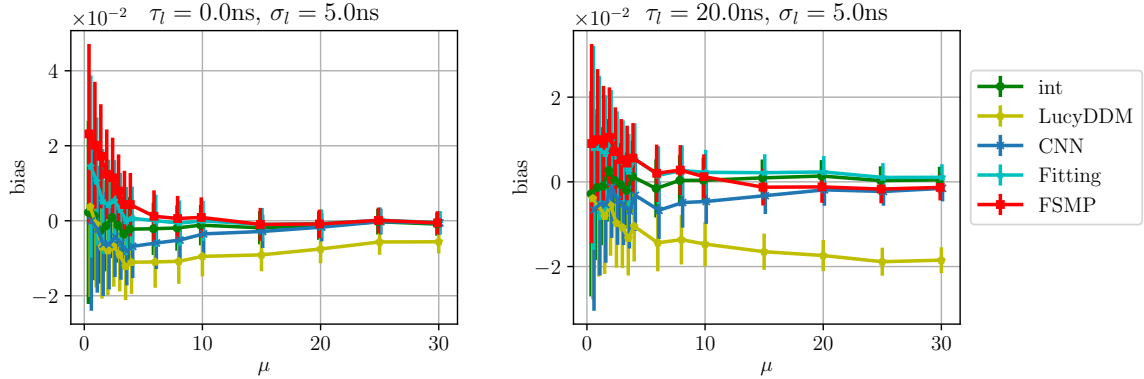
The message is clear from figure 15b: any PMT-based experiment that relies on time with PMT occupancy  $\mu$  larger than 3 should employ waveform analysis.



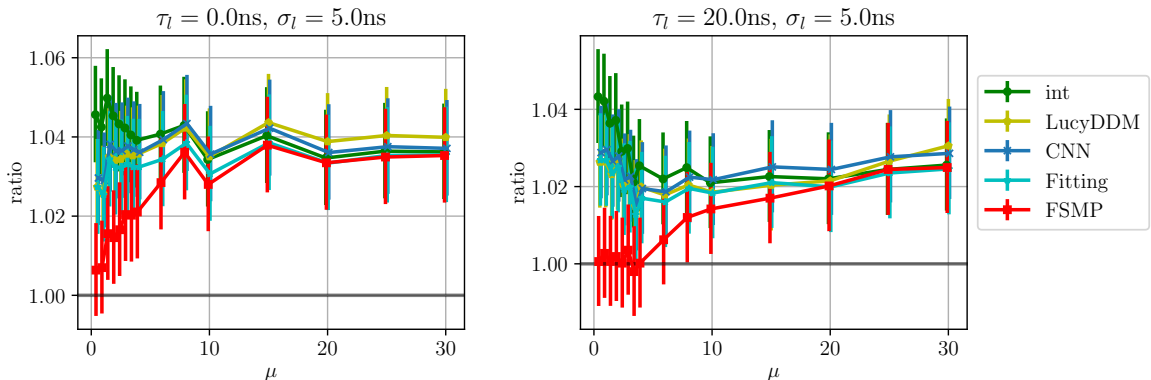
(a) Sample average of time reconstruction biases  $\overline{\Delta t}$ , where  $\Delta t = \hat{t} - t_0$ .



(b) Ratios of resolution  $\sigma_{\hat{t}_0}/\sigma_{\text{ALL}}$  for time reconstruction. “1st” is a reproduction of figure 3.



(c) Relative sample average of intensity reconstruction biases  $\overline{\Delta \mu}/\mu$ , where  $\Delta \mu = \hat{\mu} - \mu$ .



(d) Ratios of resolution  $\sigma_{\hat{\mu}}/\sigma_{\mu} \left(1 + \frac{\Delta \mu}{\mu}\right)$  for intensity reconstruction. The factor  $1 + \frac{\Delta \mu}{\mu}$  neutralizes biases of  $\hat{\mu}$ .

Figure 15: Incident light analysis results for the two typical cases of Cherenkov (left) and scintillation (right). “ALL” and “1st” are the  $\hat{t}_{\text{ALL}}$  estimator defined in eq. (6). “int” is the  $\hat{\mu}_Q$  by eq. (7). LucyDDM, Fitting, CNN use eqs. (11) and (12). FSMP has its own natural  $\hat{t}_0$  and  $\hat{\mu}$  estimators in eq. (29).  $\sigma_{\mu} = \sqrt{\mu}$  is the lower bound of intensity resolution (section 2.3.2). Error bars are 5–95 percentiles.

In contrast to time, inference of light intensity uses empty waveforms as well. We append the waveform samples by  $10^4 \times e^{-\mu}/(1 - e^{-\mu})$  empty ones. The number is proportional to the Poisson prediction. It is equivalent to appending the same amount of zeros to the  $\hat{\mu}$ 's. The QDC integration estimator  $\hat{\mu}_Q$  (“int” in figures 15c and 15d) is ubiquitous and is plotted together with the four waveform analysis methods.

In figure 15c, the biases of  $\hat{\mu}$  of the four methods are within 2% and disappear for large  $\mu$  except LucyDDM. The tendency of LucyDDM comes from the thresholding and scaling in eq. (18). For low  $\mu$ , the upward bias of FSMP and Fitting is due to PE granularity. The charge  $q$  of one PE can fluctuate close to 2 or 0, but eqs. (24) and (29) favor 2 more than 0 in waveforms. We shall leave the amendment of the bias to event reconstruction in our subsequent publications.

For large  $\mu$  the four methods are similar in intensity resolution to  $\hat{\mu}_Q$  (figure 15d). The resolution ratios of them all approach  $1.03 = \sqrt{1 + 0.25^2}$ , consistent with eq. (8) if white noise is ignored. For small  $\mu$ , FSMP gives the best resolution by correctly modeling charge distributions, as predicted in figure 14. Like the hit estimator  $\hat{\mu}_{\text{hit}}$  in section 2.3.2, it eliminates the influence of  $\sigma_q$  and  $\sigma_\epsilon$  in eq. (8). But unlike  $\hat{\mu}_{\text{hit}}$ , FSMP also works well for a few PEs. More importantly, it provides a smooth transition from the “hit mode” to the “charge mode” with the best intensity resolution of all. In the scintillation case of figure 15d, FSMP approaches the resolution lower bound  $\sigma_\mu$  set by the PE truths for  $\mu < 5$ , which is the ultimate waveform analysis in that we can hardly do any better.

In the fluid-based neutrino and dark matter experiments,  $\mu < 5$  is the sweet spot for MeV and keV physics respectively. The intensity resolution boost in figure 15d converts directly into energy resolution. It varies depending on PMT models for different  $\sigma_q$  and  $\sigma_\epsilon$ . In our scintillation setup, the improvement is up to  $\times 1.04$  (figure 15d). Good waveform analysis has the potential to accelerate discovery and broaden the physics reach of existing detectors.

## 5 Conclusion

We develop and compare a collection of waveform analysis methods. We show for  $N_{\text{PE}} > 1$ , better time resolution can be achieved than the first PE hit time. FSMP gives the best accuracy in both time and intensity measurements, while CNN, Fitting and LucyDDM follow. We find significant time ( $\times 2$ ) and intensity ( $\times 1.04$ ) resolution improvements at higher and lower light intensities, respectively. FSMP opens the opportunity to boost energy resolution ( $\times 1.04$ ) and particle identification in PMT-based neutrino and dark matter experiments. We invite practitioners to deploy FSMP for the best use of the data and tune it for faster execution.

## Acknowledgments

We are grateful to the participants and organizers of the *Ghost Hunter 2019* online data contest. CNN, Fitting and LucyDDM in this article are developed from the ones submitted to the contest. We would like to thank Changxu Wei and Wentai Luo for sharing findings on direct charge fitting. The idea of multivariate Gaussian emerged during a consulting session at the Center for Statistical Science at Tsinghua University. The authors also want to thank Professor Kai Uwe Martens for discussions on PE granularity. The corresponding author would like to express deep gratitude to KamLAND, XMASS and JUNO collaborations for nurturing atmosphere and encouraging discussions on waveform analysis. This work is supported in part by the National Natural Science Foundation of China (11620101004), the Key Laboratory of Particle & Radiation Imaging (Tsinghua University).

## References

- [1] The Super-Kamiokande Collaboration, *The Super-Kamiokande detector, Nuclear Instruments and Methods in Physics Research Section A: Accelerators, Spectrometers, Detectors and*

*Associated Equipment* **501** (2003) 418.

- [2] J. Dunger, *Event Classification in Liquid Scintillator Using PMT Hit Patterns: for Neutrinoless Double Beta Decay Searches*, Springer Theses. Springer International Publishing, Cham, 2019, 10.1007/978-3-030-31616-7.
- [3] Daya Bay Collaboration, *Measurement of electron antineutrino oscillation based on 1230 days of operation of the Daya Bay experiment*, *Physical Review D* **95** (2017) 072006.
- [4] KamLAND Collaboration, *Production of radioactive isotopes through cosmic muon spallation in KamLAND*, *Physical Review C* **81** (2010) 025807.
- [5] G. Alimonti, C. Arpesella, H. Back, M. Balata, D. Bartolomei, A. de Bellefon et al., *The Borexino detector at the Laboratori Nazionali del Gran Sasso*, *Nuclear Instruments and Methods in Physics Research Section A: Accelerators, Spectrometers, Detectors and Associated Equipment* **600** (2009) 568.
- [6] K. Abe, K. Hieda, K. Hiraide, S. Hirano, Y. Kishimoto, K. Kobayashi et al., *XMASS detector*, *Nuclear Instruments and Methods in Physics Research Section A: Accelerators, Spectrometers, Detectors and Associated Equipment* **716** (2013) 78.
- [7] XENON Collaboration, *XENON1T dark matter data analysis: Signal reconstruction, calibration, and event selection*, *Physical Review D* **100** (2019) 052014.
- [8] H. Q. Zhang, Z. M. Wang, Y. P. Zhang, Y. B. Huang, F. J. Luo, P. Zhang et al., *Comparison on PMT waveform reconstructions with JUNO prototype*, *Journal of Instrumentation* **14** (2019) T08002.
- [9] M. Li, Z. Guo, M. Yeh, Z. Wang and S. Chen, *Separation of scintillation and Cherenkov lights in linear alkyl benzene*, *Nuclear Instruments and Methods in Physics Research Section A: Accelerators, Spectrometers, Detectors and Associated Equipment* **830** (2016) 303.
- [10] S. Jetter, D. Dwyer, W.-Q. Jiang, D.-W. Liu, Y.-F. Wang, Z.-M. Wang et al., *PMT waveform modeling at the Daya Bay experiment*, *Chinese Physics C* **36** (2012) 733.
- [11] S. Levy and P. K. Fullagar, *Reconstruction of a sparse spike train from a portion of its spectrum and application to high-resolution deconvolution*, *GEOPHYSICS* **46** (1981) 1235.
- [12] M. Mihoko and S. Eguchi, *Robust Blind Source Separation by Beta Divergence*, *Neural computation* **14** (2002) 1859.
- [13] E. Levina and P. Bickel, *The Earth Mover's distance is the Mallows distance: some insights from statistics*, in *Proceedings Eighth IEEE International Conference on Computer Vision. ICCV 2001*, vol. 2, pp. 251–256 vol.2, July, 2001, DOI.
- [14] A. Savitzky and M. J. E. Golay, *Smoothing and Differentiation of Data by Simplified Least Squares Procedures.*, *Analytical Chemistry* **36** (1964) 1627.
- [15] L. B. Lucy, *An iterative technique for the rectification of observed distributions*, *The Astronomical Journal* **79** (1974) 745.
- [16] M. Li, G.-W. Li, K. Lv, F.-Q. Duan, H. Haerken and Y.-H. Zhao, *The Richardson-Lucy deconvolution method to extract LAMOST 1D spectra*, *Research in Astronomy and Astrophysics* **19** (2019) 145.
- [17] K. He, X. Zhang, S. Ren and J. Sun, *Deep Residual Learning for Image Recognition*, in *2016 IEEE Conference on Computer Vision and Pattern Recognition (CVPR)*, pp. 770–778, June, 2016, DOI.

- [18] A. Vaswani, N. Shazeer, N. Parmar, J. Uszkoreit, L. Jones, A. N. Gomez et al., *Attention Is All You Need*, *arXiv:1706.03762 [cs]* (2017) .
- [19] M. Slawski and M. Hein, *Non-negative least squares for high-dimensional linear models: Consistency and sparse recovery without regularization*, *Electronic Journal of Statistics* **7** (2013) 3004.
- [20] R. H. Byrd, P. Lu, J. Nocedal and C. Zhu, *A Limited Memory Algorithm for Bound Constrained Optimization*, *SIAM Journal on Scientific Computing* **16** (1995) 1190.
- [21] R. M. Neal, *MCMC using Hamiltonian dynamics*, *arXiv:1206.1901 [physics, stat]* (2012) .
- [22] P. Schniter, L. C. Potter and J. Ziniel, *Fast bayesian matching pursuit*, in *2008 Information Theory and Applications Workshop*, pp. 326–333, Jan., 2008, DOI.
- [23] N. Metropolis, A. W. Rosenbluth, M. N. Rosenbluth, A. H. Teller and E. Teller, *Equation of State Calculations by Fast Computing Machines*, *J. Chem. Phys.* **21** (1953) 1087.
- [24] W. K. Hastings, *Monte Carlo sampling methods using Markov chains and their applications*, *Biometrika* **57** (1970) 97.
- [25] D. J. C. MacKay, v. J. C. MacKay and D. J. C. M. Kay, *Information Theory, Inference and Learning Algorithms*. Cambridge University Press, Sept., 2003.
- [26] R.-B. Chen, C.-H. Chu, T.-Y. Lai and Y. N. Wu, *Stochastic matching pursuit for Bayesian variable selection*, *Statistics and Computing* **21** (2011) 247.
- [27] C. Ekanadham, D. Tranchina and E. P. Simoncelli, *Recovery of Sparse Translation-Invariant Signals With Continuous Basis Pursuit*, *IEEE Transactions on Signal Processing* **59** (2011) 4735.
- [28] C. J. Geyer and J. Møller, *Simulation Procedures and Likelihood Inference for Spatial Point Processes*, *Scandinavian Journal of Statistics* **21** (1994) 359.